Supporting Information

Electrolytic Gold Plating, Stripping, and Ion Transport Dynamics Through A Solid-State Iodide Perovskite

Tuo Hu,[a] *Ross A. Kerner*,[b*] *Aishwarya Singh*,[c] *Yutong Ren*,[a] *Ayala V. Cohen*,[c] *Antoine Kahn*,[a] *Leeor Kronik*,[c] *Qiangfei Xia*,[d] and *Barry P. Rand*[a,e*]

[a] Department of Electrical and Computer Engineering, Princeton University, Princeton, NJ 08544, USA

[b] Chemistry and Nanoscience Center, National Renewable Energy Laboratory, Golden, CO 80401, USA

[c] Department of Molecular Chemistry and Materials Science, Weizmann Institute of Science, Rehovoth 76100, Israel

[d] Department of Electrical and Computer Engineering, University of Massachusetts, Amherst, MA 01003, USA

[e]Andlinger Center for Energy and the Environment, Princeton University, Princeton, NJ 08544, USA

[*]Correspondence: ross.kerner@nrel.gov (R.A.K.) and brand@princeton.edu (B.P.R.)

Methods

Materials and Sample Fabrication: Lead iodide (PbI_2, 99.99% trace metal basis) and methylammonium iodide (MAI, > 99.99) were purchased from TCI and GreatCell Solar respectively. N,N-dimethylformamide (DMF, anhydrous, 99.8%), and chlorobenzene (CB, anhydrous, 99.8%) were purchased from Sigma-Aldrich. 3 × 3 cm^2 patterned indium tin oxide (ITO) substrates were purchased from Colorado Concept Coatings. All materials and solvents were used as received.

0.8 M $MAPbI_3$ precursor solutions were prepared in a N_2-filled glovebox by dissolving appropriate molar ratios of PbI_2 and MAI in DMF:

- 10% MAI-excess: 0.80 M PbI_2 + 0.88 M MAI
- Stoichiometric: 0.80 M PbI_2 + 0.80 M MAI
- 10% MAI-deficient: 0.80 M PbI_2 + 0.72 M MAI

Different perovskite thicknesses are achieved by varying the concentrations of the precursor solutions (i.e., 0.50 M and 1.2 M).

Patterned ITO substrates were cleaned by sequential sonication in detergent, deionized water, acetone and isopropanol for 10 min each, followed by a 10 min O_2-plasma treatment immediately prior to perovskite deposition. Perovskite precursor solution was spin-coated in a N_2-filled glovebox on the as-cleaned ITO substrates via a two-step program: 1000 rpm for 10 s with a ramping rate of 1000 rpm/s, followed by 6000 rpm for 30 s with a ramping rate of 2000 rpm/s. 100 μL of CB as an antisolvent was dropped onto the substrate 25 s before the end of the entire spin-coating program. The samples were immediately annealed on a 100 ^oC hotplate for 30 min. Devices were completed by thermal evaporation of 100 nm of Au through a shadow mask defining 12 pixels per substrate, each with an active area of ~0.1 cm^2 (4 × 2.5 mm^2).

Characterization:

Current density versus time (*J-t*) characteristics were measured using a Keithley 2602B sourcemeter controlled by SCPI Matlab scripts. All *J-t* transients were measured in a N_2 environment in the dark at room temperature.

X-ray spectroscopy (XPS) measurements were performed by a Thermo-Scientific Kα X-ray Photoemission Spectrometer operating at a base pressure of $<1 \times 10^{-7}$ mbar and using an Al anode at a power of 72 W. Scanning electron microscopy (SEM) images were measured by an FEI Verios 460 XHR SEM. Samples were coated with 3 nm of Iridium before SEM measurements.

Density Functional Theory (DFT) Computation:

All DFT calculations were performed using the Vienna ab initio simulation package (VASP),[1] a plane-wave basis code in which ionic cores are described by the projected augmented wave (PAW) method.[2] All calculations were performed using a 2×2×2 (385 atoms) supercell of tetragonal $MAPbI_3$ (a=b=8.88 Å, c=12.64 Å), with a 2×2×1 K-point mesh to sample the Brillouin zone. Au defects were introduced by placing Au atoms at conventional iodine interstitial sites, with charge removed to create Au^+. All structures were optimized using the Perdew-Burke-Ernzerhof (PBE) form of the generalized-gradient approximation (GGA),[3] augmented by Tkatchenko-Scheffler (TS) pair-wise dispersive terms.[4] Forces were minimized to below 0.01 eV/atom and a plane wave energy cutoff of 600 eV was used. In the ground-state structure, the Au atom is in the +1 state and is 2-coordinated to neighboring iodine ions. Nudged elastic band (NEB) calculations were performed according to the method of Henkelman *et al*.[5,6] These calculations identified the energetically favorable migration path as the one in which the defect hops from an interstitial site on the *ab*-plane to an interstitial site on the *bc*-plane. These initial and final structures were first optimized, then a linear interpolation consisting of 5 grid points between them was employed to define the migration path.

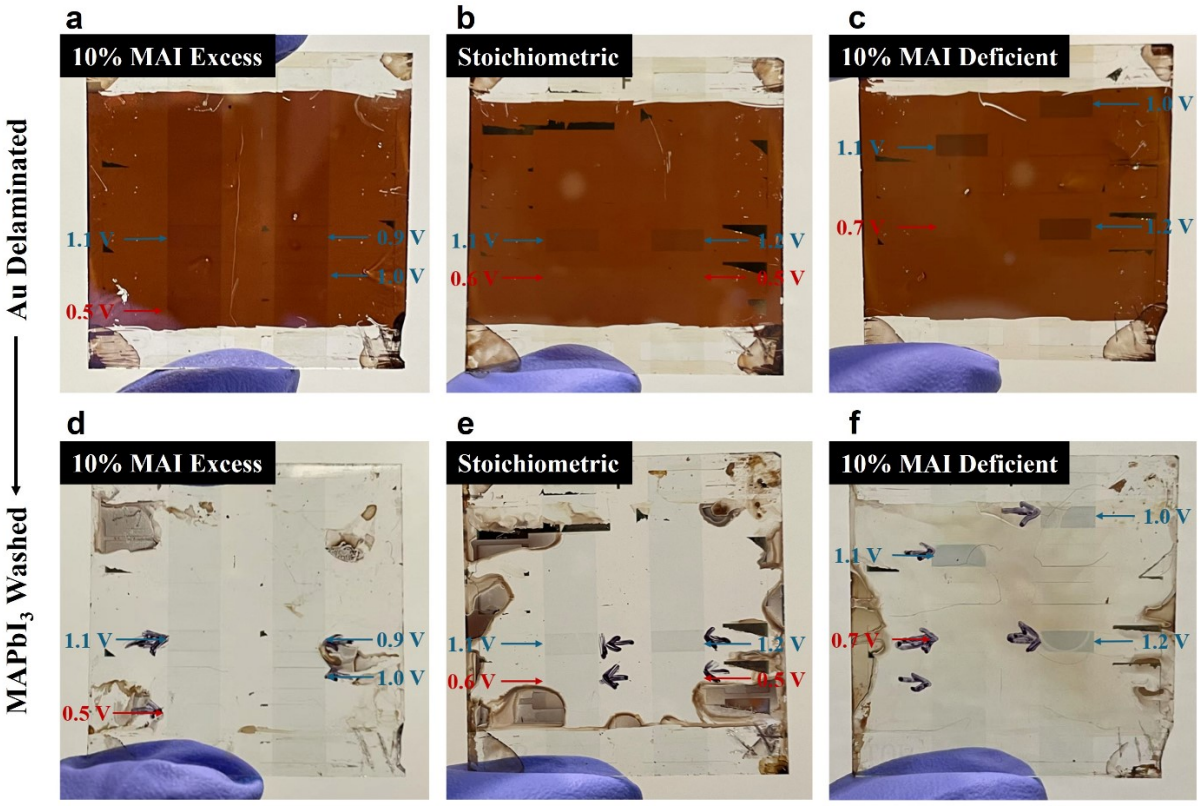

Figure S1. Photographs of 3 × 3 cm substrates hosting ITO/$MAPbI_3$/Au devices with (a,d) 10% MAI-excess, (b,e) stoichiometric, and (c,f) 10% MAI-deficient compositions after the 2 h potentiostatic biasing test. Pictures were taken (a-c) after Au delamination with tape and (d-f) after washing the perovskite layer away. Pixels biased at representative voltages are indicated by arrows, where blue and red denote suprathreshold and subthreshold biasing conditions respectively.

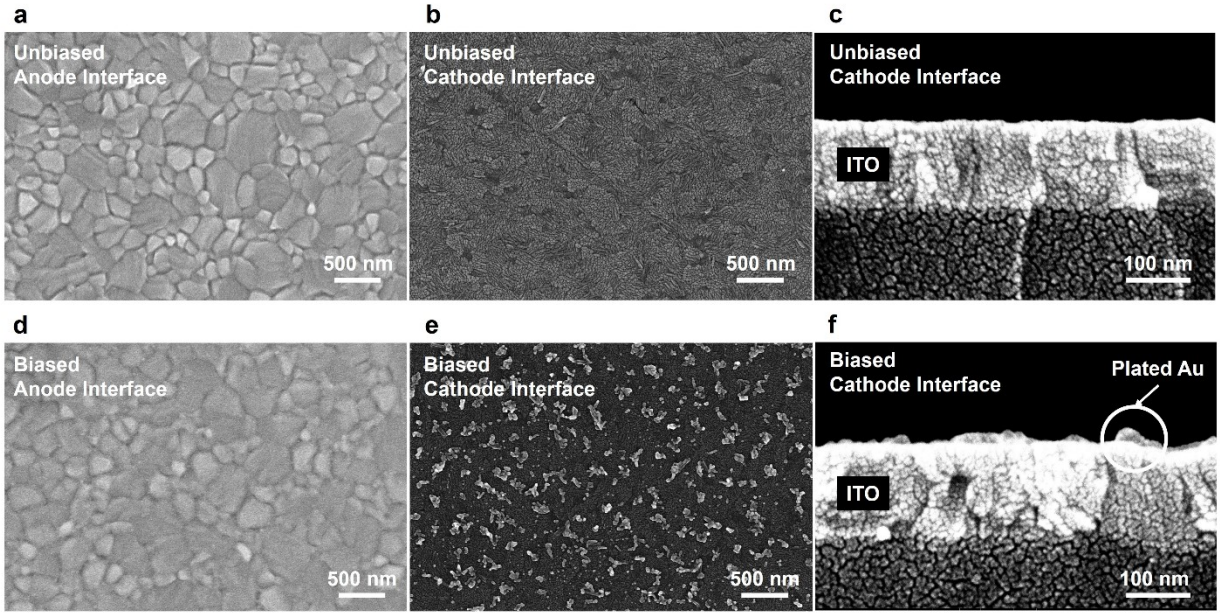

Figure S2. SEM images of ITO/stoichiometric $MAPbI_3$/Au devices before and after 2 h biasing at 1.2 V. Surface SEM images at the top $MAPbI_3$ interface after Au delamination of an (a) unbiased and (d) biased pixel. Surface SEM images at the ITO interface after washing off $MAPbI_3$ of an (b) unbiased and (e) biased pixel. Cross-sectional SEM images of the ITO layer after washing off $MAPbI_3$ of an (b) unbiased and (e) biased pixel.

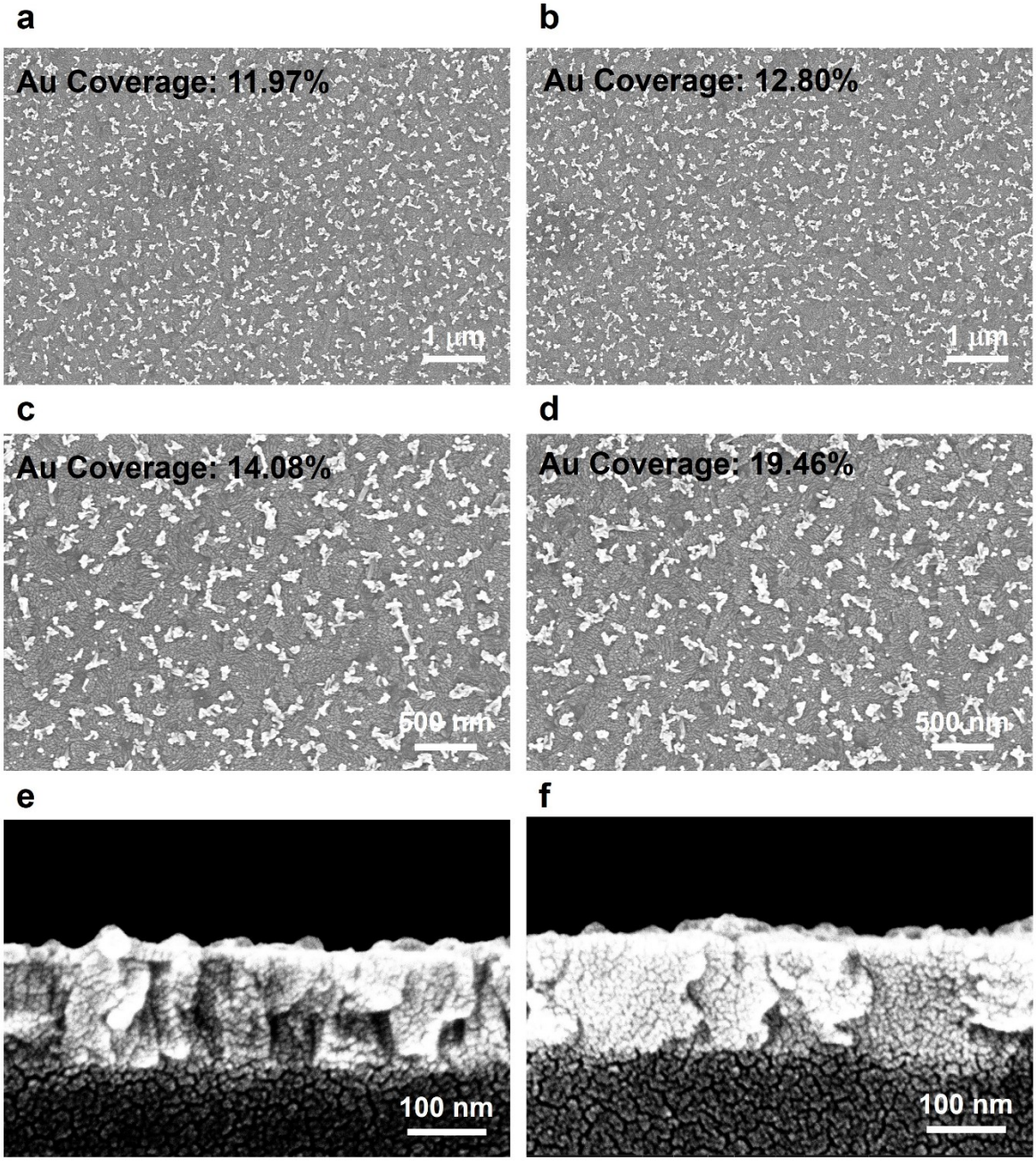

Figure S3. Additional SEM images of ITO/stoichiometric $MAPbI_3$/Au devices after 2 h biasing at 1.2 V. (a-d) Surface and (e,f) cross-sectional SEM images at different locations on the ITO layer after Au delamination.

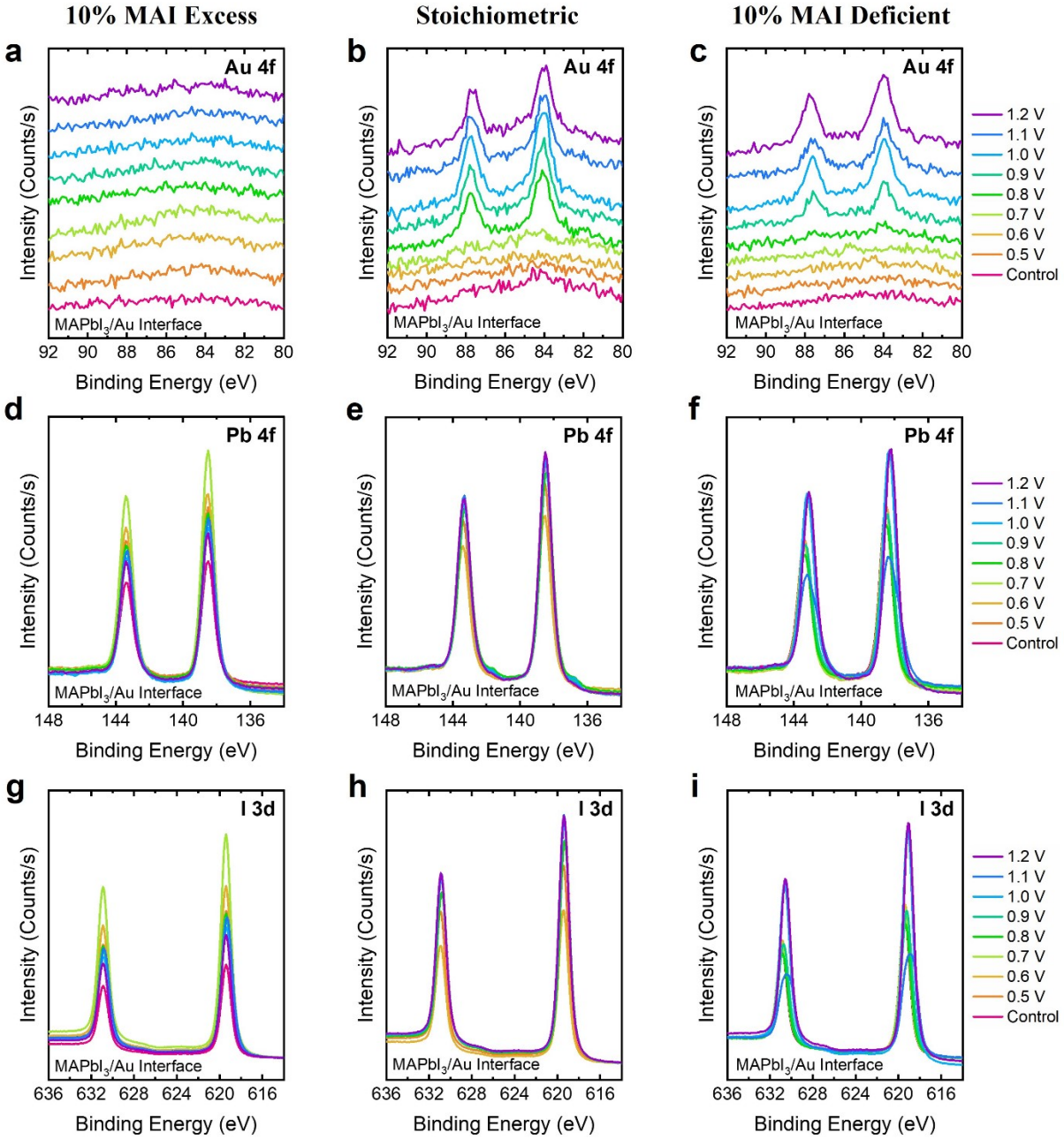

Figure S4. XPS measurements at the top $MAPbI_3$ interface after Au delamination of ITO/$MAPbI_3$/Au devices with (a,d,g) 10% MAI-excess, (b,e,h) stoichiometric, and (c,f,i) 10% MAI-deficient compositions after biasing at various voltages for 2 h: (a-c) Au 4f, (d-f) Pb 4f, and (g-i) I 3d spectra. The control device was under no bias at all.

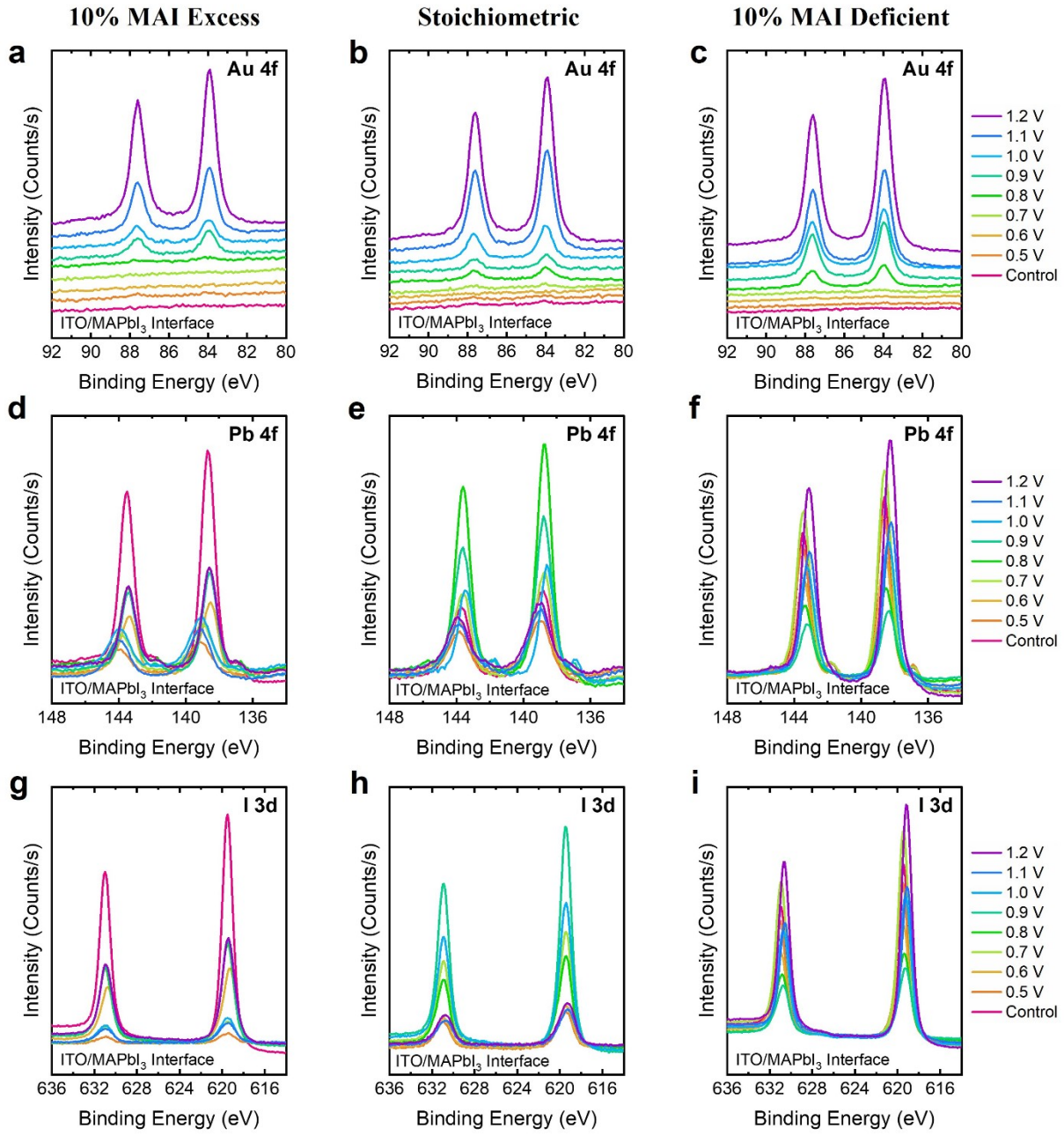

Figure S5. XPS measurements at the bottom ITO interface after washing off the perovskite layer of ITO/$MAPbI_3$/Au devices with (a,d,g) 10% MAI-excess, (b,e,h) stoichiometric, and (c,f,i) 10% MAI-deficient compositions after biasing at various voltages for 2 h: (a-c) Au 4f, (d-f) Pb 4f, and (g-i) I 3d spectra. The control device was under no bias at all.

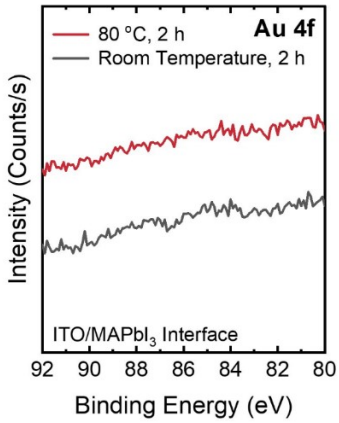

Figure S6. XPS measurements at the bottom ITO interface after removing the perovskite layer in ITO/stoichiometric $MAPbI_3$/Au devices thermally aged at 80 °C for two hours. This temperature was deliberately chosen to replicate the estimated temperature due to Joule heating at 100 mA/cm^2 in a 4 × 2.5 mm^2 device.[7] A control device stored at room temperature is included for reference. No Au 4f signal is detected in the aged device, confirming that elevated temperature alone is insufficient to drive gold migration across the perovskite layer on this timescale.

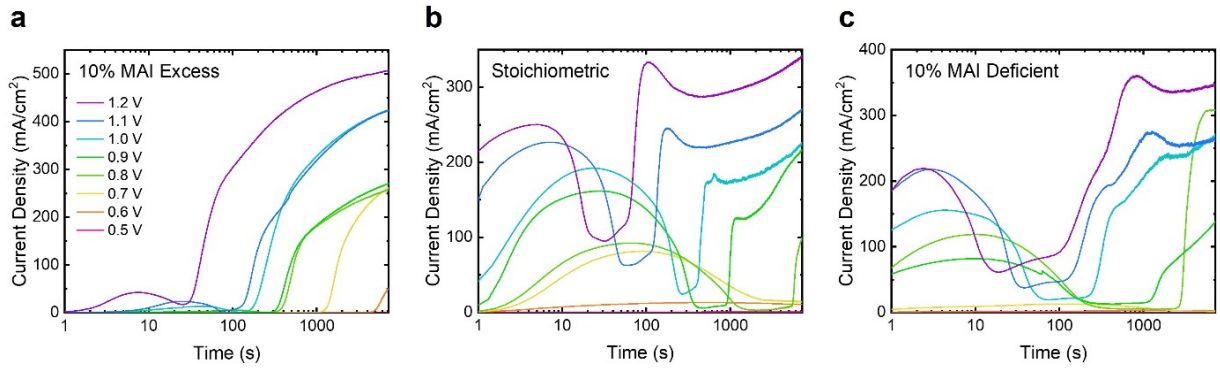

Figure S7. Current-density versus time (*J-t*) characteristics of (a) ITO/10% MAI-excess $MAPbI_3$/Au, (b) ITO/stoichiometric $MAPbI_3$/Au, and (c) ITO/10% MAI-deficient $MAPbI_3$/Au devices at indicated voltages for 2 h.

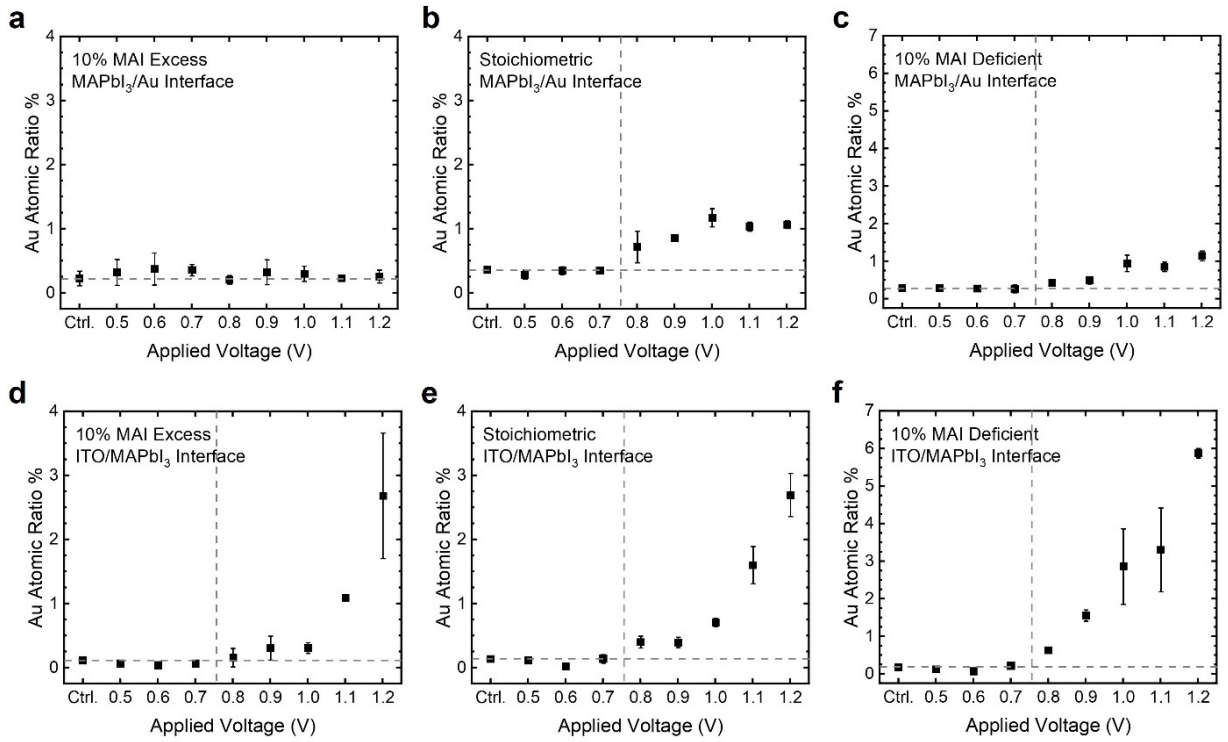

Figure S8. Au atomic percentage as a function of applied voltage calculated from XPS results for ITO/$MAPbI_3$/Au devices with (a,d) 10% MAI-excess, (b,e) stoichiometric, and (c,f) 10% MAI-deficient compositions: (a-c) at the top $MAPbI_3$ interface after Au delamination and (d-f) at the bottom ITO interface after washing off the perovskite layer. At least three points were measured for each biasing condition for statistical relevance. Error bars reflect the standard deviation of Au atomic percentages measured by XPS. The horizontal gray dashed lines provide visual reference of the control level, and the vertical gray dashed lines refer to the onset of detectable Au signals in XPS spectra.

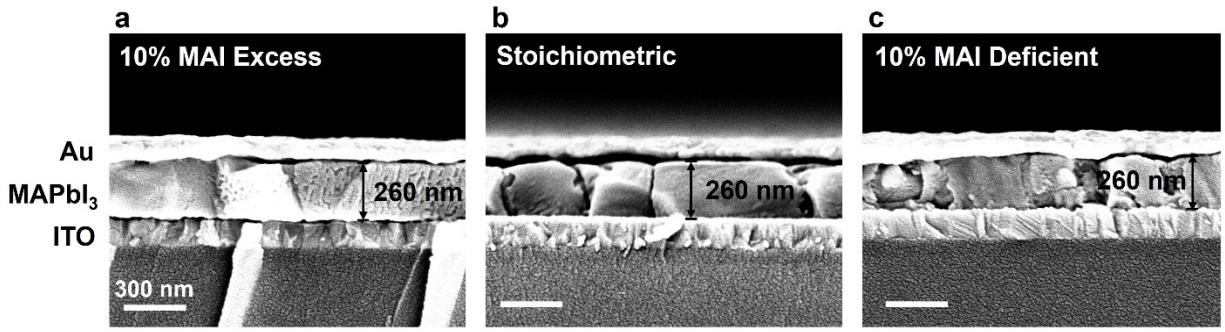

Figure S9. Cross-sectional SEM images of as-fabricated (a) ITO/10% MAI-excess $MAPbI_3$/Au, (b) ITO/stoichiometric $MAPbI_3$/Au, and (c) ITO/10% MAI-deficient $MAPbI_3$/Au devices. The perovskite layer thickness is measured to be consistent at approximately 260 nm across different stoichiometries.

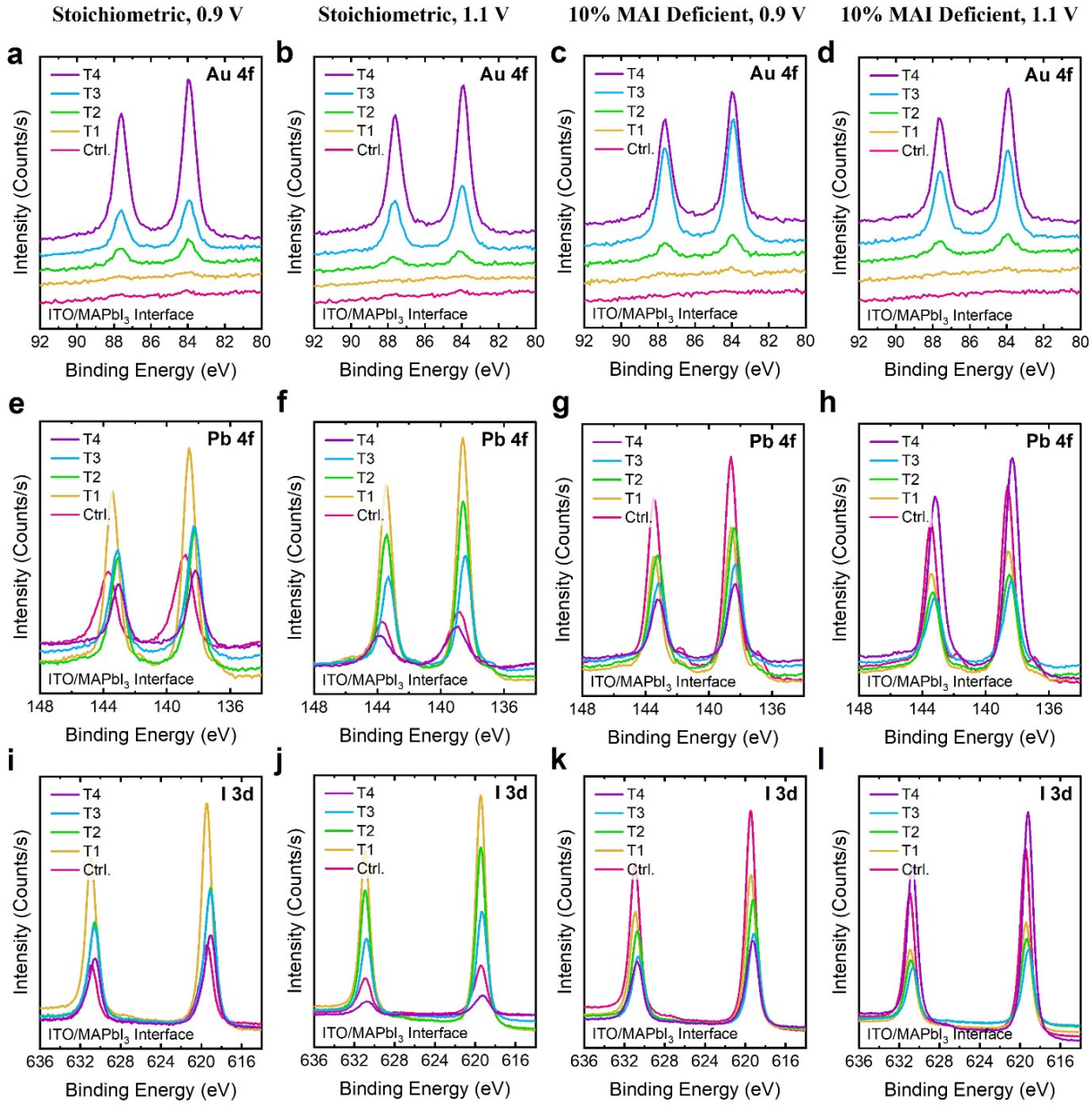

Figure S10. XPS measurements at the bottom ITO interface after washing off the perovskite layer in devices subjected to potentiostatic biasing till specified time points: (a-d) Au 4f, (e-h) Pb 4f, and (i-l) I 3d spectra. Devices include: (a,e,i) ITO/stoichiometric $MAPbI_3$/Au biased at 0.9 V, (b,f,j) ITO/stoichiometric $MAPbI_3$/Au biased at 1.1 V, (c,g,k) ITO/10% MAI-deficient $MAPbI_3$/Au biased at 0.9 V, and (d,h,l) ITO/10% MAI-deficient $MAPbI_3$/Au biased at 1.1 V.

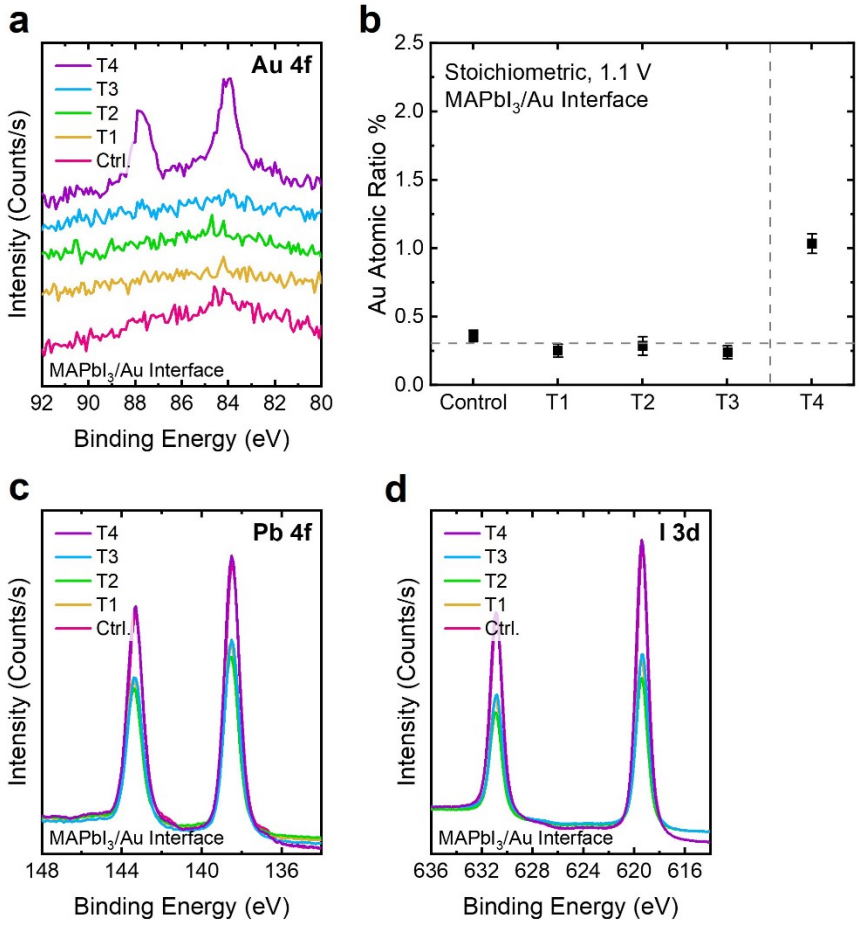

Figure S11. XPS measurements at the top $MAPbI_3$ interface of ITO/stoichiometric $MAPbI_3$/Au devices at each characteristic time point (T1-T4) during potentiostatic biasing at 1.1 V: (a) Au 4f, (c) Pb 4f, and (d) I 3d spectra. (b) Au atomic percentage at each time point calculated from XPS results. At least three points were measured for each biasing condition for statistical relevance. Error bars reflect the standard deviation of Au atomic percentages measured by XPS. The horizontal gray dashed lines provide visual reference of the control level, and the vertical gray dashed lines refer to the onset of detectable Au signals in XPS spectra.

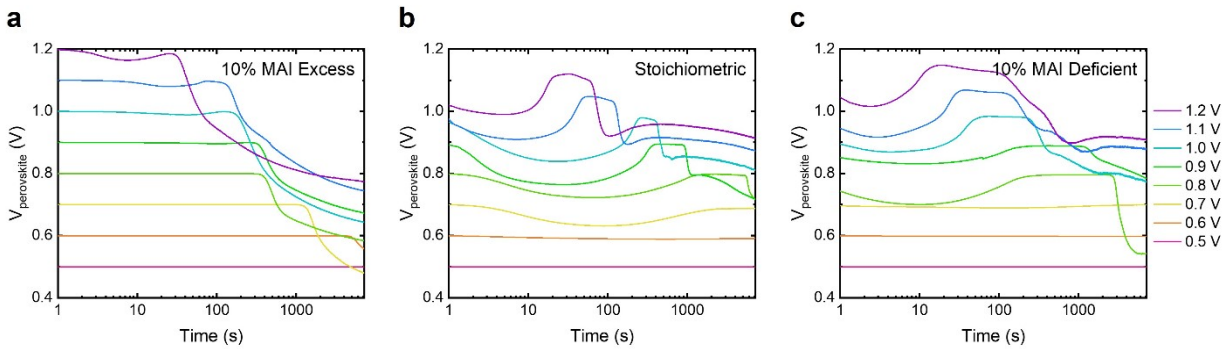

Figure S12. Actual voltage across the perovskite layer ($V_{perovskite}$) for (a) ITO/10% MAI-excess $MAPbI_3$/Au, (b) ITO/stoichiometric $MAPbI_3$/Au, and (c) ITO/10% MAI-deficient $MAPbI_3$/Au devices at various applied voltages during the potentiostatic measurements. $V_{perovskite}$ is calculated by $V_{perovskite} = V_{applied} - I \times R_{ITO}$, where $V_{applied}$ is the total voltage applied on the device, I is the measured current, and R_{ITO}, estimated to be 8.4 Ω, is the series resistance of the ITO. $V_{perovskite}$ drops well below the 0.8 V threshold during the later stages of biasing in MAI-excess devices, which may account for the absence of detectable Au signal at the top $MAPbI_3$/Au interface after 2 hours of biasing. $V_{perovskite}$ is comparable in the stoichiometric and the MAI-deficient devices before T2, allowing meaningful comparison of Au migration kinetics between the two compositions.

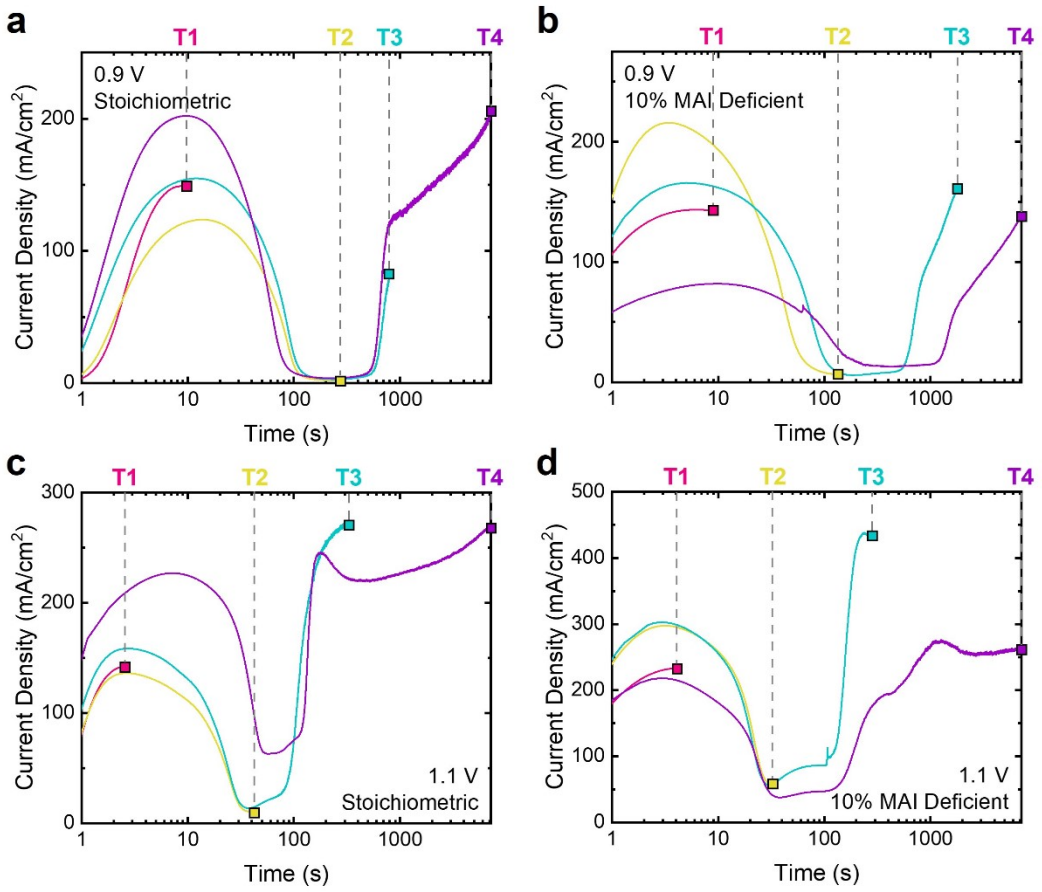

Figure S13. *J-t* transients stopped at each of the 4 characteristic time points (T1-T4) during potentiostatic biasing of (a,c) ITO/stoichiometric $MAPbI_3$/Au and (b,d) ITO/10% MAI-deficient $MAPbI_3$/Au devices under two representative voltages: (a,b) 0.9 V and (c,d) 1.1 V. Each *J-t* curve was collected on a fresh pixel.

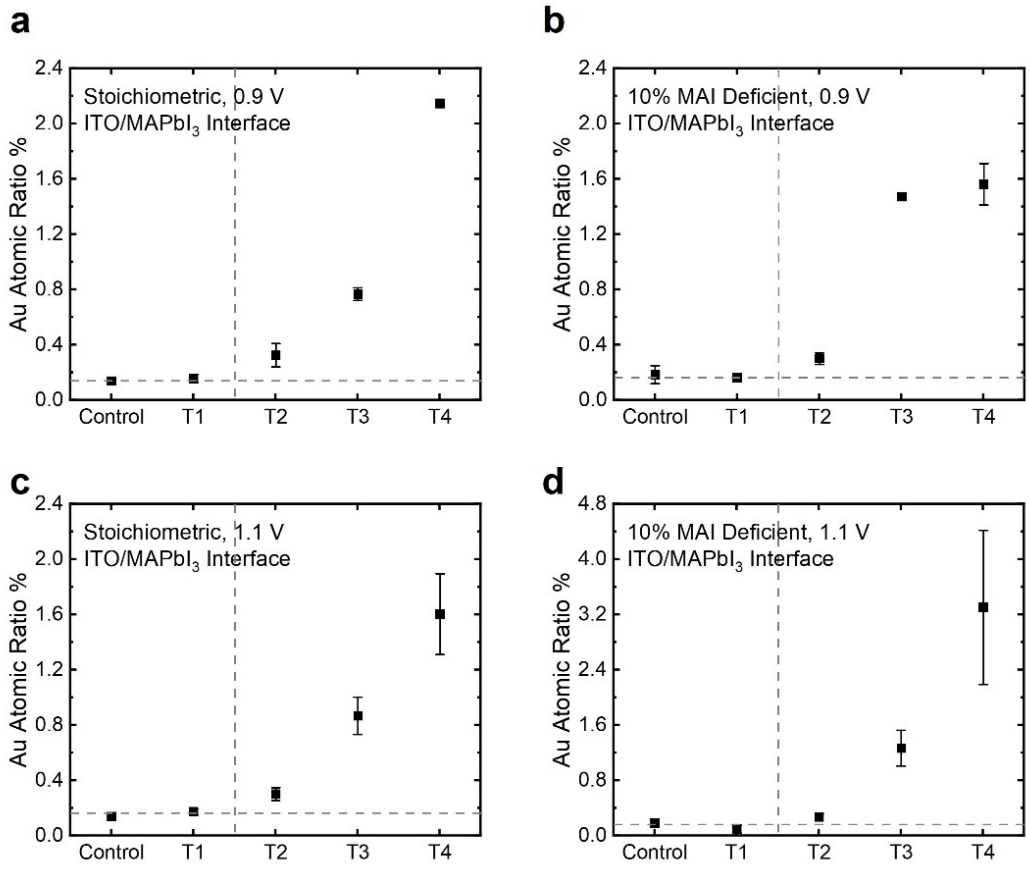

Figure S14. Au atomic percentage as a function of characteristic time points during potentiostatic biasing calculated from XPS results for ITO/$MAPbI_3$/Au devices, including (a) ITO/stoichiometric $MAPbI_3$/Au biased at 0.9 V, (b) ITO/10% MAI-deficient $MAPbI_3$/Au biased at 0.9 V, (c) ITO/stoichiometric $MAPbI_3$/Au biased at 1.1 V, and (d) ITO/10% MAI-deficient $MAPbI_3$/Au biased at 1.1 V. At least three points were measured for each biasing condition for statistical relevance. Error bars reflect the standard deviation of Au atomic percentages measured by XPS. The horizontal gray dashed lines provide visual reference of the control level, and the vertical gray dashed lines refer to the onset of detectable Au signals in XPS spectra.

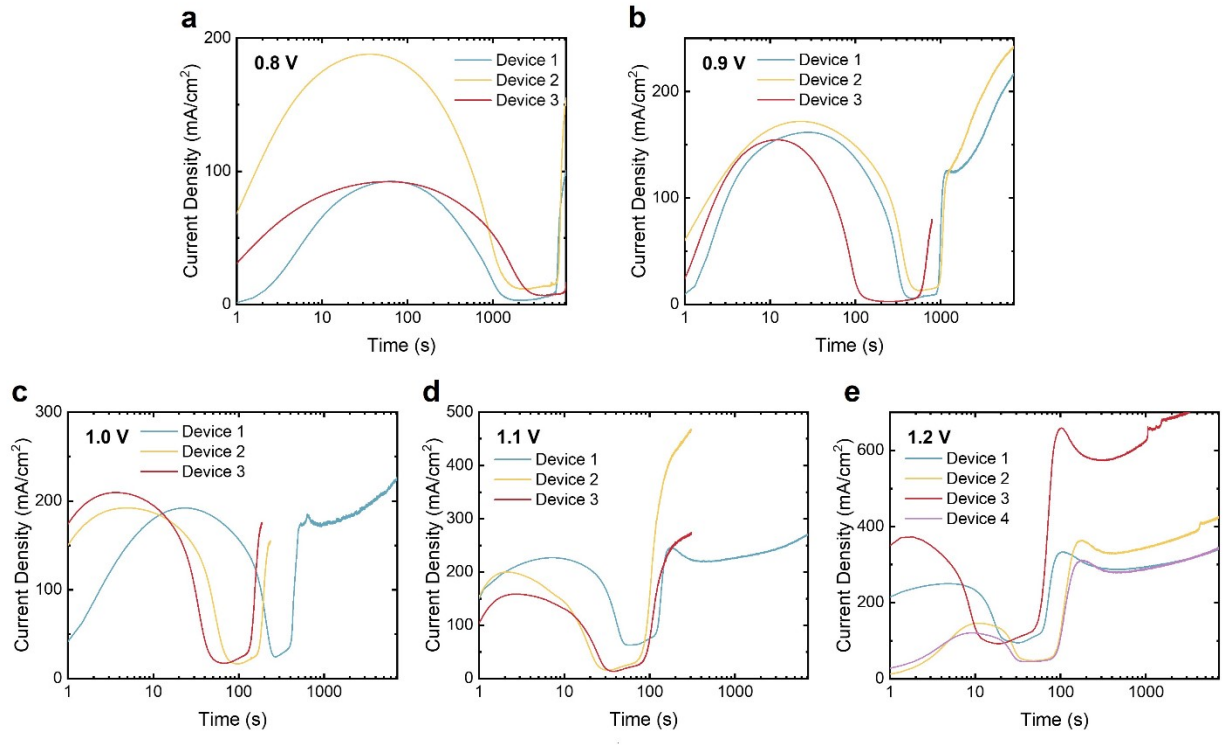

Figure S15. *J-t* transients of ITO/stoichiometric $MAPbI_3$/Au devices biased at (a) 0.8 V, (b) 0.9 V, (c) 1.0 V, (d) 1.1 V, and (e) 1.2 V. Each figure includes *J-t* curves from at least three individual fresh pixels.

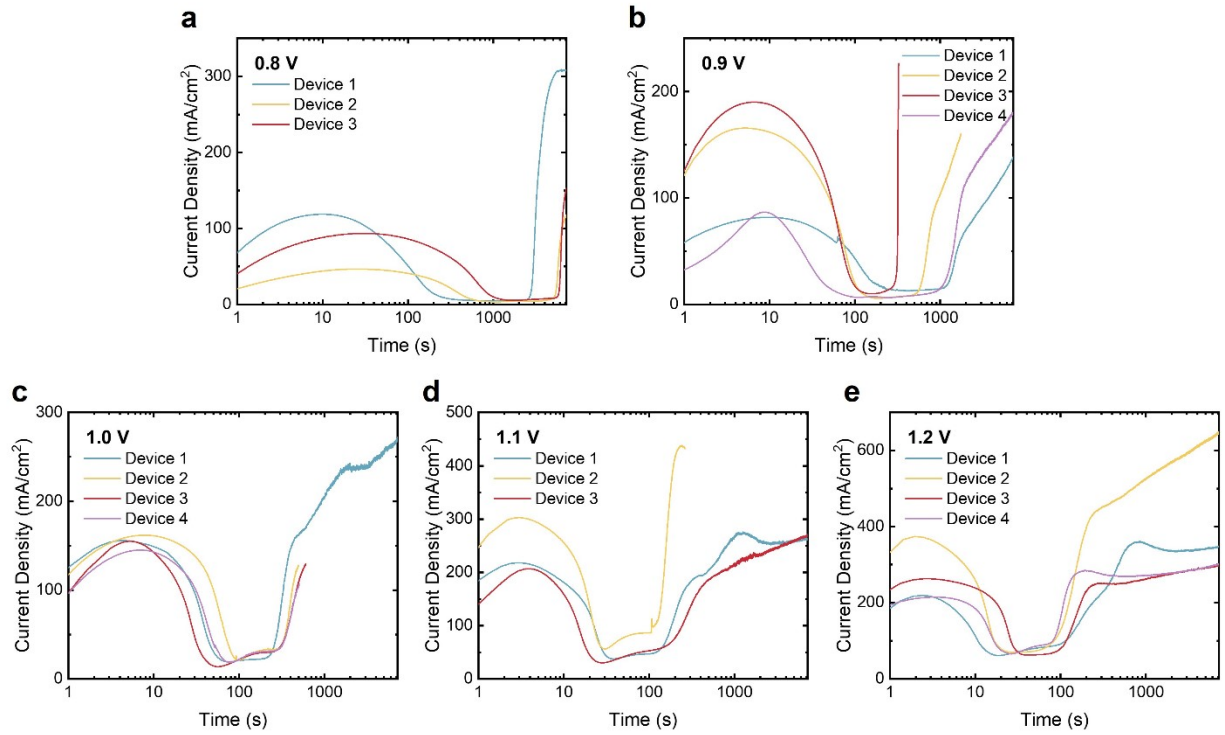

Figure S16. *J-t* transients of ITO/10% MAI-deficient $MAPbI_3$/Au devices biased at (a) 0.8 V, (b) 0.9 V, (c) 1.0 V, (d) 1.1 V, and (e) 1.2 V. Each figure includes *J-t* curves from at least three individual fresh pixels.

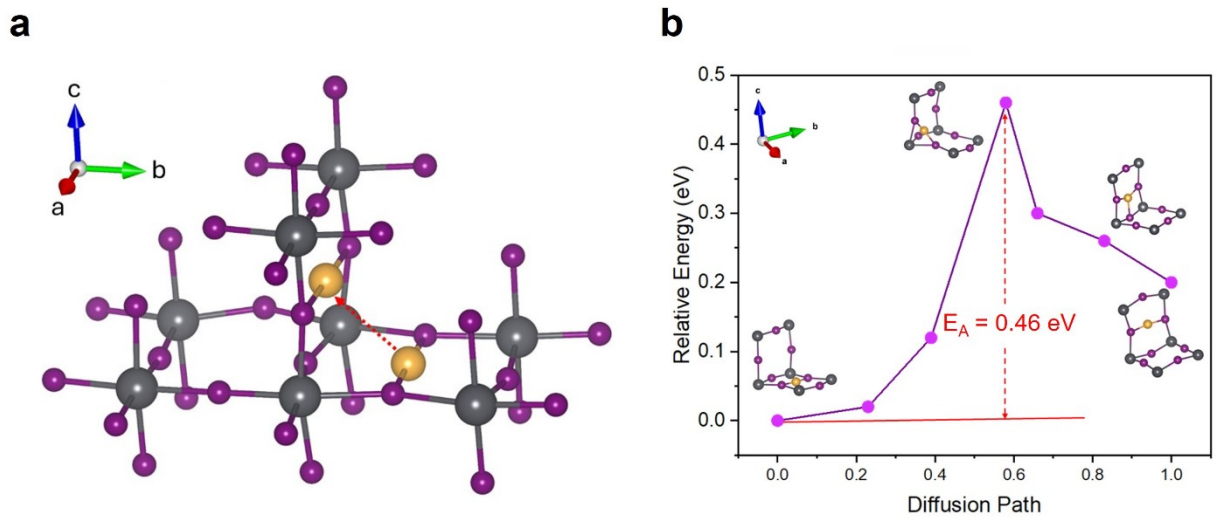

Figure S17. (a) Schematic of the gold interstitial cation (Au_i^+, yellow atom) diffusion pathway in $MAPbI_3$ (methylammonium omitted for clarity). The Au cation hops from an interstitial site on the *ab*-plane (initial) to one on a *bc*-plane (final). The distance between the relaxed initial and final Au_i^+ positions is found to be 5.16 Å. (b) Energy path of Au_i^+ migration, obtained from DFT calculations using the NEB method. Representative transition states during the migration process are included. The relative energy is defined as the total energy difference between each transition state and the initial configuration. The activation energy (E_A), defined by the highest-energy transition state, is found to be 0.46 eV.

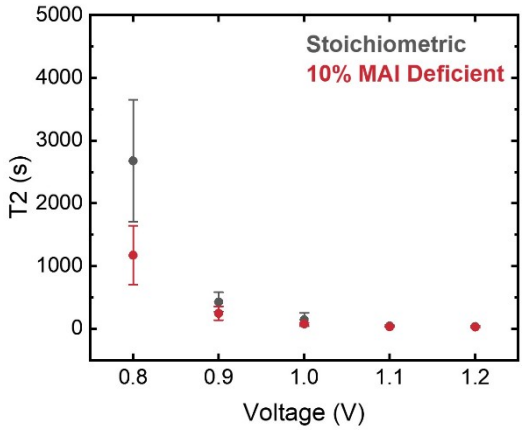

Figure S18. T2 values as a function of applied voltage for both stoichiometric and 10% MAI-deficient devices, plotted on a linear y-axis. T2 values are extracted from *J-t* transients shown in Figure S15 and S16. Error bars reflect the standard deviation of T2 values among at least three individual pixels per condition. Numerical values are summarized in Table S1.

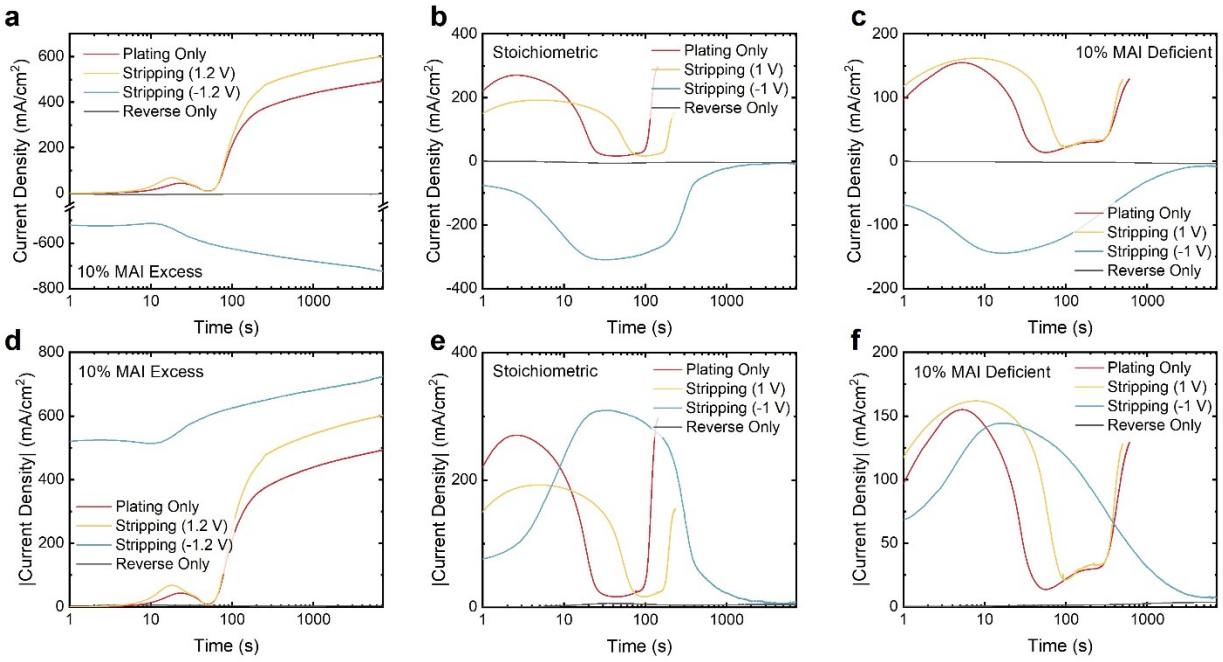

Figure S19. *J-t* transients of ITO/$MAPbI_3$/Au devices with (a,d) 10% MAI-excess, (b,e) stoichiometric, and (c,f) 10% MAI-deficient compositions during Au plating and stripping processes. Plots show (a-c) measured current density or (d-f) magnitude of current density versus time.

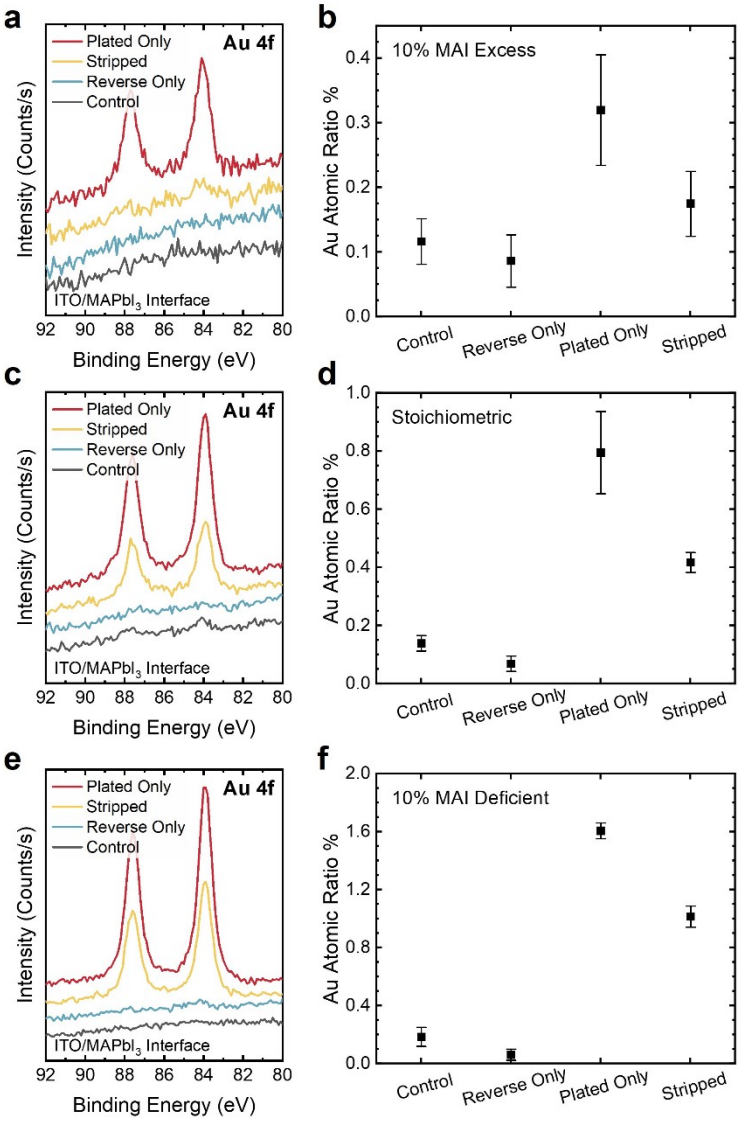

Figure S20. XPS measurements at the bottom ITO interface after washing off the perovskite layer of ITO/stoichiometric $MAPbI_3$/Au devices with (a,b) 10% MAI-excess, (c,d) stoichiometric, and (e,f) 10% MAI-deficient compositions: (a,c,e) Au 4f spectra and (b,d,f) Au atomic percentage calculated from the XPS results. The "plated-only" device was biased at 1 V till T3; the "stripped" device was biased at 1 V till T3 immediately followed by a 2 h biasing at −1 V; the "reverse-only" device was biased at −1 V for 2 h; and the "control" was never under any stressing. Error bars reflect the standard deviation of Au atomic percentages measured by XPS.

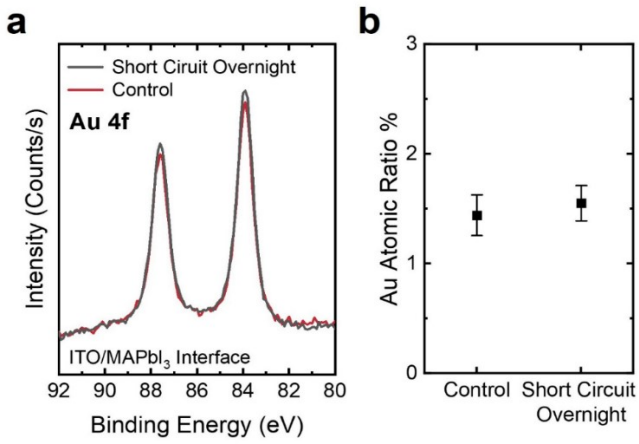

Figure S21. XPS measurements at the bottom ITO interface after removing the perovskite layer from two ITO/stoichiometric $MAPbI_3$/Au devices plated under 1 V for 2 hours, one of which was left at short circuit overnight: (a) Au 4f spectra and (b) Au atomic percentages for each sample. Error bars in (b) reflect the standard deviation of Au atomic percentages from three data points per sample.

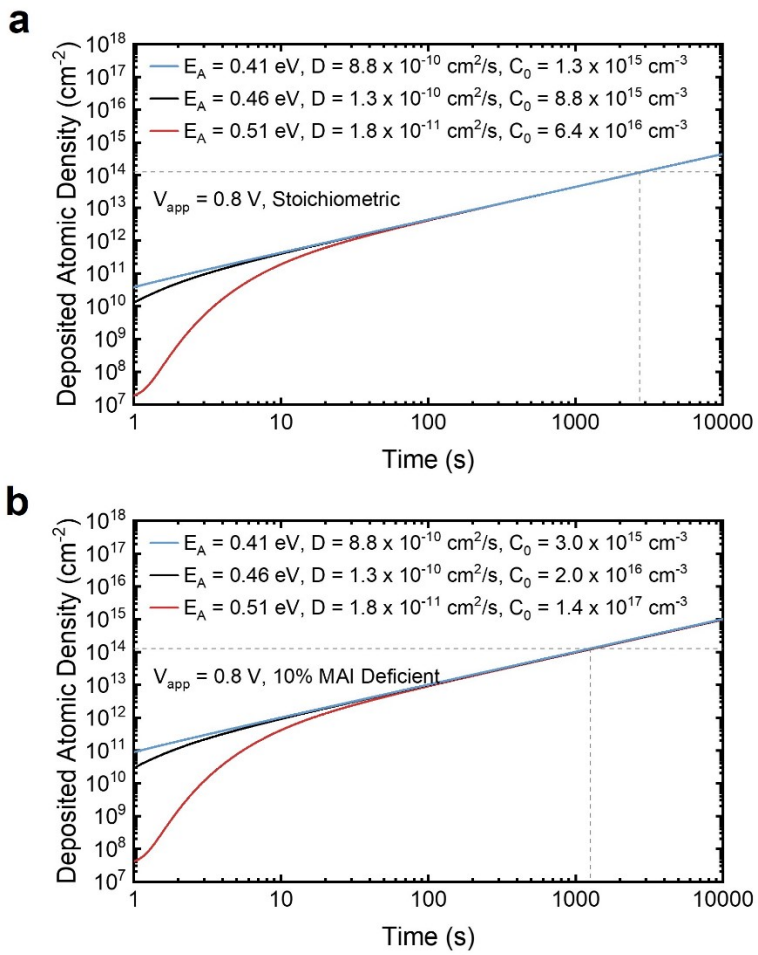

Figure S22. Simulated Au atomic density deposited at the ITO interface over time, using the theoretical diffusion coefficient range (1.8×10^{-11} to 8.8×10^{-10} cm^2/s) to extract the corresponding range of Au_i^+ concentrations at the top interface (C_0) for (a) a stoichiometric and (b) a 10% MAI-deficient device at 0.8 V. The diffusion coefficients are calculated based on the DFT-derived migration barrier for Au_i^+ in $MAPbI_3$ (E_A = 0.46 ± 0.05 eV). Gray dashed lines mark the onset concentration for detectable Au plated at the ITO. Additional simulation details are provided in Note S2.

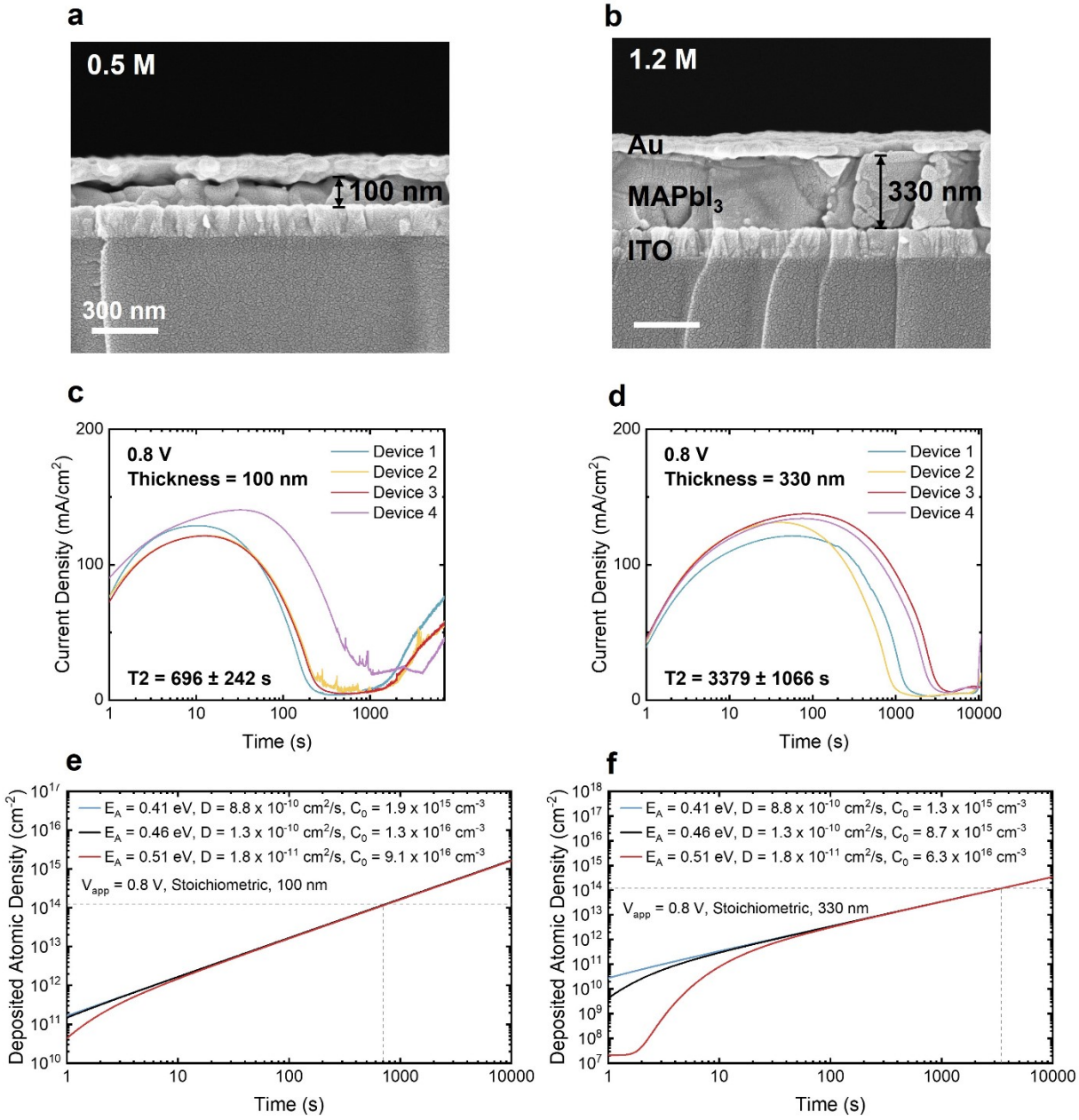

Figure S23. Diffusion modelling of ITO/stoichiometric $MAPbI_3$/Au devices with different perovskite thicknesses. Cross-sectional SEM images of as-fabricated devices with (a) 100 nm and (b) 330 nm $MAPbI_3$. *J-t* transients at 0.8 V for devices with (c) 100 nm and (d) 330 nm $MAPbI_3$. Simulated Au atomic density deposited at the ITO interface over time, using the theoretical diffusion coefficient range (1.8×10^{-11} to 8.8×10^{-10} cm^2/s) to extract C_0 for (e) 100 nm and (f) 330 nm $MAPbI_3$ devices at 0.8 V.

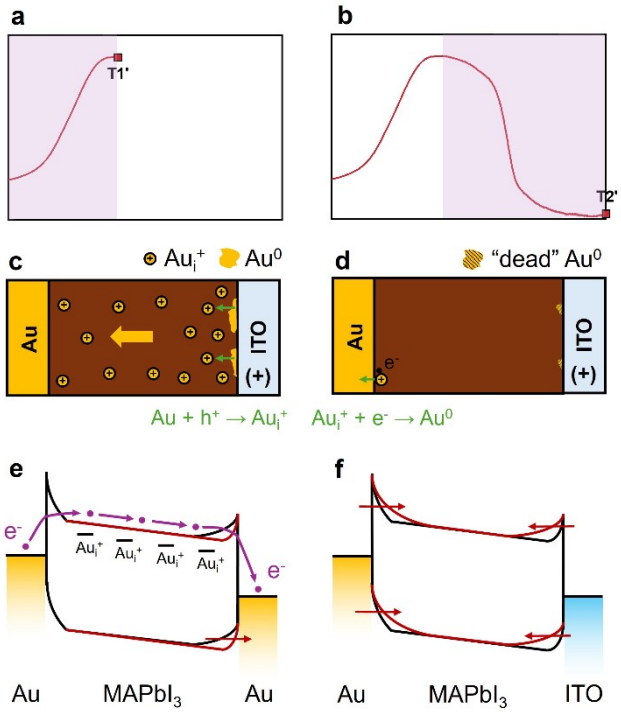

Figure S24. Proposed model rationalizing the current transient features during the stripping process. Each column corresponds to one of the two characteristic time points (T1' and T2'). (a,b) Representative current-time transients during stripping, highlighting each characteristic time point and conduction stages between them, with the purple shading representing electron-dominated conduction. (c,d) Schematics of qualitative Au spatial distribution at each time point. (e,f) Corresponding qualitative device energy diagrams.

Table S1. T2 values in the *J-t* transients of ITO/$MAPbI_3$/Au devices under potentiostatic biasing at various voltages.

	0.8 V	**0.9 V**	**1.0 V**	**1.1 V**	**1.2 V**
Stoichiometric	2678 ± 973 s	428 ± 155 s	146 ± 108 s	45 ± 16 s	36 ± 13 s
10% MAI Def.	1173 ± 467 s	247 ± 108 s	78 ± 16 s	33 ± 5 s	28 ± 9 s

Note S1. Contribution of ionic current carried by Au_i^+ transport to the total current during potentiostatic biasing.

The total charge passed through the device during the potentiostatic biasing is obtained by integrating the current density for the 1.2 V transient in Figure 1b over the entire 2 h biasing period, yielding 2.27×10^6 mC/cm^2. Since each plated Au atom consumes one electron for the reduction reaction ($Au_i^+ + e^- \rightarrow Au^0$), the total ionic current associated with Au_i^+ transport can be estimated from the amount of Au^0 accumulated on the ITO interface after the 2 h biasing. Surface SEM image analysis (Figure S3) reveals an average Au coverage of 14.58% after. Approximating the plated Au islands as tetragonal with an average thickness of 10 nm (per cross-sectional SEM images in Figure S2), and assuming the atomic density of crystalline Au (5.91×10^{22} cm^{-3}), the corresponding area atomic density of plated Au is calculated to be 8.62×10^{15} cm^{-2}. This translates to a total charge of 1.38 mC/cm^2 over 2 hours due to ionic charge transfer. It means that the ionic current due to Au_i^+ transport accounts for only ~1/(6.07×10^7) of the total charge, confirming its negligible contribution and highlighting the predominantly electronic nature of the current transients observed in Figure 1b.

Note S2. Au_i^+ diffusion coefficients and doping concentrations in $MAPbI_3$ based on DFT calculations and the experimental estimation based on the temporal onset of Au plating on ITO (T2).

The theoretical Au_i^+ diffusivity can be estimated based on the vibration frequency of Au-I^- bonds. The diffusion coefficient for ion migration can be written as

$$D = D_0 \cdot \exp\left(-\frac{E_A}{kT}\right) = \left(\frac{z}{6}\right) a^2 \mu \cdot \exp\left(-\frac{E_A}{kT}\right)$$

where z represents the number of equivalent migration sites, a is the jump distance between sites, μ is the attempt frequency, and E_A is the migration activation energy. As illustrated in Figure S17a, there are 4 equivalent migration sites for Au_i^+ within the $MAPbI_3$ lattice (z = 4), and the jump distance is roughly 5.16 Å (a = 5.16 Å). Because Au_i^+ migration involves breaking and reforming Au-I^- bonds, the vibrational frequency of these bonds represents the attempt frequency, which has been reported to be around 150 cm^{-1}, corresponding to 4.5 THz in frequency, based on surface-enhanced Raman spectroscopy (SERS) measurements (μ = 4.5 THz).[8] Furthermore, we performed density functional theory (DFT) simulations to model the energy profile associated with Au_i^+ migration (Figure S17b), yielding an activation energy of 0.46 ± 0.05 eV (E_A = 0.46 ± 0.05 eV), which aligns well with the previously reported value.[9] With these values, the theoretical Au_i^+ diffusion coefficients can be calculated to be in the range of 1.8×10^{-11} to 8.8×10^{-10} cm^2/s.

Using the theoretical diffusion coefficients, we can estimate the Au_i^+ doping concentration at the anode interface based on the temporal onset of Au plating on ITO (T2) combined with diffusion modeling. According to "Mathematics of Diffusion" by Crank,[10] the total amount of diffusion species per unit area (Q(t)) crossing the boundary at $x = L$ as a function of time is described as:

$$Q(t) = \frac{D(C_0 - C_L)t}{L} + \frac{2L}{\pi^2}\sum_{n=1}^{\infty}\frac{C_0\cos(n\pi) - C_L}{n^2}\left[1 - \exp\left(-\frac{Dn^2\pi^2 t}{L^2}\right)\right] + \frac{4C_i L}{\pi^2}\sum_{m=1}^{\infty}\frac{}{(2}$$

where D is the diffusion coefficient of the diffusing species. In this analysis, the top $MAPbI_3$/Au interface is defined as position x = 0 nm while the bottom ITO/$MAPbI_3$ interface is defined as position $x = L$ = 260 nm, where the thickness of the perovskite film (L) is measured from the cross-

sectional SEM images (Figure S9). The interface $x = 0$ is assumed to be at a constant concentration C_0 and the other interface $x = L$ at a constant C_L, and it starts with a uniform concentration of C_i throughout the system. During the early stage of Au_i^+ diffusion in our case, we assume that C_L and C_i are both zero, i.e., there is no Au_i^+ in the perovskite at $t = 0$, and the cathodic reaction is fast enough that all Au_i^+ cations are immediately reduced to Au^0 once they reach ITO. With these assumptions, the above equation is reduced to:

$$Q(t) = \frac{DC_0 t}{L} + \frac{2LC_0}{\pi^2} \sum_{n=1}^{\infty} \frac{cos(n\pi)}{n^2} \left[1 - \exp\left(-\frac{Dn^2\pi^2 t}{L^2}\right)\right]$$

which allows us to simulate the amount of deposited Au on ITO as a function of time given a certain diffusion coefficient and interfacial doping concentration C_0, as shown in Figure S22.

According to Figure S14, at the onset of Au plating (T2), the atomic Au percentage at the ITO interface is measured to be approximately 0.3% for all biasing conditions. Considering that each ITO unit cell contains 80 atoms and has a lattice constant of a = 1.012 nm,[11] and assuming an X-ray penetration depth of 5 nm, this 0.3% Au atomic concentration on ITO corresponds to a surface density of Q(T2) = 1.16 $\times 10^{14}$ cm^{-2}. As depicted in Figure S22, by matching this value (indicated by the horizontal gray dashed lines) with the experimental T2 values at a specific biasing condition using the theoretical diffusion coefficients, we can extract the C_0 values. This results in a C_0 range of 1.3 × 10^{15} to 1.4 × 10^{17} cm^{-3}, aligning with reported defect densities in polycrystalline perovskites (10^{15}-10^{17} cm^{-3}),[12-14] which supports the reliability of our diffusion modeling and analysis.

Importantly, we need to note that our experimental estimation assumes a purely diffusive regime where the concentration gradient is the only driving force for Au_i^+ transport. To further validate the pure-diffusion model, we extended the kinetics analysis to devices with different perovskite thicknesses (100 and 330 nm, Figure S23a and S23b). Four pixels per thickness were biased at threshold (0.8 V) to obtain statistically meaningful T2 values (Figure S23c and S23d). Note that the threshold was shown to be independent of perovskite thickness.[15] Following the aforementioned methodology and assuming the same diffusivity range, we can extract the C_0 values for each thickness (Figure S23e and S23f). This yields a C_0 range of 1.9 × 10^{15} to 9.1 × 10^{16} cm^{-3} for the 100 nm-thick devices and 1.3 × 10^{15} to 6.3 × 10^{16} cm^{-3} for the 330 nm devices, aligning consistently with the 260 nm samples (1.3 × 10^{15} to 6.4 × 10^{16} cm^{-3}). Given the thickness-

independent nature of C_0, this result demonstrates that our diffusion model reliably captures Au migration kinetics across different perovskite thicknesses under threshold bias, further confirming our pure-diffusion assumption is adequate under threshold voltage biasing conditions to minimize the electric field in the perovskite. While it does not completely rule out the migration of Au_i^+ by an electric field, we have done our best to minimize this effect. More complex drift-diffusion modelling in future work is needed to fully confirm the results, and our work here provides a quantitative estimate for D and realistic C_0 ranges upon which to build these models.

However, in our biasing experiment, when the applied bias exceeds the threshold voltage, a portion of that voltage is likely dropped across the neutral region of the perovskite bulk. This voltage drop, which increases with higher applied biases, leads to an electric filed aligned with Au_i^+ migration. As a result, field-driven drift may accelerate ion migration, which is one of the reasons for the reduction in T2 values at elevated voltages. To minimize the effects of such drift and ensure the validity of the diffusion-based model, we restrict our analysis to the threshold voltage condition (0.8 V), where most of the applied bias is expected to drop across the $MAPbI_3$/Au interface for the electrochemical reaction, making the internal voltage drop across the perovskite layer negligible. A similar logic should be adopted when applying this method to determine diffusion coefficients for other extrinsic metal ions in perovskites. It thus emphasizes the critical importance of accurately identifying the electrochemical threshold voltage at various perovskite/metal interfaces.

In addition to the field-driven drift that complicates proper modeling at suprathreshold biasing conditions, it is hard to accurately quantify the concentration of Au_i^+ at the top interface (C_0) under different applied voltages. We believe that C_0 should be exponentially dependent on the applied voltage, as described by the following equation:

$$C_0 = C^o \cdot exp(\frac{-\Delta G + eV_{app}}{kT})$$

where C^o is the concentration of neutral Au^0 atoms at the top interface available for the oxidation reaction, ΔG is the Gibbs free energy change for Au_i^+ formation, V_{app} is the applied voltage, k is Boltzmann's constant, and T is the temperature. Our earlier work shows that ΔG for Au_i^+ formation depends on the Fermi energy, and thus it is a function of the applied bias.[16] This adds further complexity to the accurate estimation of C_0, placing it beyond the scope of the current study.

Nevertheless, this relation suggests that C_0 increases with the applied bias, resulting in a higher concentration of Au_i^+ at elevated voltages and consequently a faster Au_i^+ transport. The combined effects of enhanced field-driven drift and increased C_0 at higher applied biases likely lead to the observed empirical linear correlation between the natural logarithm of average T2 values and the applied voltage (Figure 2c). However, a complete understanding of Au_i^+ transport under suprathreshold conditions will require a more detailed investigation into the interfacial concentration boundary conditions, spatial electric field distribution, and the voltage dependence of ΔG for Au_i^+ formation.

Even with these limitations of our model in mind, it is worth emphasizing that this approach offers a straightforward means to estimate the diffusivity of extrinsic metal ions in perovskites and may be readily extended to other metals, such as Ag or Cu, across different perovskite compositions. As shown by Ming et al., DFT computations indicate that when Ag or Cu incorporates into $MAPbI_3$, these metal species predominantly exist as monovalent cations at interstitial sites within the perovskite lattice, analogous to Au_i^+.[9] The identical oxidation state and bonding environment suggest that Ag_i^+ and Cu_i^+ are likely generated or discharged through similar redox reactions, impose comparable doping/de-doping effects, and migrate within the $MAPbI_3$ lattice via mechanisms akin to Au_i^+. These parallels make our kinetic model and analysis directly generalizable to Ag and Cu. Differences in migration kinetics among the three metals in $MAPbI_3$ arise primarily from variations in defect formation energies and migration barriers. Specifically, Ming et al. reported that the formation enthalpy curves of Ag_i^+ and Cu_i^+ shift to lower values relative to Au_i^+, with Ag_i^+ being the lowest,[9] suggesting that Ag_i^+ and Cu_i^+ oxidation and migration may occur at lower threshold voltages. This is logical given the differences in the metals' oxidation potentials in aqueous electrolytes.[17] In the same study, the migration barrier of Cu_i^+ is found to be comparable to Au_i^+, whereas the barrier for Ag_i^+ is 0.15 eV lower.[9] It suggests that Cu_i^+ likely migrates at rates similar to Au_i^+, while Ag_i^+ can diffuse up to two orders of magnitude faster, consistent with our previous findings.[16]

Note S3. Proposed mechanistic interpretation of the current transient features during the stripping process.

As shown in Figure 2a, the plating current transient exhibits three characteristic features: an initial current increase (T1), a subsequent low trough (T2), and a later second rise (T3). Similarly, the stripping transient reproduces the first two features: it begins with an initial current rise to a maximum (T1', Figure S24a) and then falls to a low-current plateau (T2', Figure S24b). The only difference is that the stripping process does not display the final current increase seen in plating. To rationalize the stripping current transient, a mechanistic interpretation is presented in Figure S24, including the proposed energy-diagram model for each characteristic time point (T1' and T2') during the stripping process.

During stripping under a positive bias at the ITO electrode, plated Au experiences an anodic environment where they are oxidized to Au_i^+ cations that re-enter the perovskite lattice (Figure S24c). This injection of Au_i^+ significantly increases the dopant concentration at the bottom interface, narrowing the Schottky junction depletion width at the plated-Au/$MAPbI_3$ interface (Figure S24c) and contributing to the initial current increase via enhanced electron tunneling (Figure S24a). Meanwhile, the cathodic environment at the top interface releases I_{UPD}^0 species, reducing the work function of the Au electrode and facilitating electron injection. Driven by the applied field, Au_i^+ cations migrate towards the top electrode where they are reduced back to Au^0, effectively de-doping the perovskite.

As stripping proceeds, the consumption of plated Au slows the doping rate at the bottom electrode, while de-doping at the top interface starts to dominate, leading to a gradual current decrease after the first peak. Continued bias depletes the Au_i^+ dopants in the perovskite bulk (Figure S24d), rendering the film increasingly intrinsic and widening the depletion width at both interfaces (Figure S24f, red arrows). This reduction in free carriers and less favorable interfacial transport brings the current to the low plateau (Figure S24b). Further biasing no longer triggers any electrochemical reactions once Au is exhausted, consistent with the persistent low current level and the absence of a secondary rise. This differentiates from the plating process, where the Au electrode provides a virtually inexhaustible source of Au for injection into the perovskite.

References

1. G. Kresse and J. Furthmüller, *Phys. Rev. B*, 1996, **54**, 11169-11186.

2. G. Kresse and D. Joubert, *Phys. Rev. B*, 1999, **59**, 1758-1775.
3. J. P. Perdew, K. Burke and M. Ernzerhof, *Phys. Rev. Lett*., 1996, **77**, 3865-3868.
4. A. Tkatchenko and M. Scheffler, *Phys. Rev. Lett.*, 2009, **102**, 073005.
5. G. Henkelman, B. P. Uberuaga and H. Jónsson, *J. Chem. Phys*., 2000, **113**, 9901.
6. G. Henkelman and H. Jónsson, *J. Chem. Phys.*, 2000, **113**, 9978.
7. L. Zhao, K. Roh, S. Kacmoli, K. Al Kurdi, S. Jhulki, S. Barlow, S. R. Marder, C. Gmachl and B. P. Rand, *Adv. Mater.*, 2020, **32**, 2000752.
8. M. Y. Chan, W. Leng and P. J. Vikesland, *ChemPhysChem*, 2018, **19**, 24–28.
9. W. Ming, D. Yang, T. Li, L. Zhang and M. H. Du, *Adv. Sci.*, 2018, **5**, 1700662.
10. J. Crank, *Mathematics of Diffusion*, 2nd Ed. Oxford University Press: Bristol, 1975; Ch 4.
11. M. Quaas, C. Eggs and H. Wulff, *Thin Solid Films*, 1998, **332**, 277–281.
12. L. K. Ono, S. Liu and Y. Qi, *Angew. Chem. Int. Ed.*, 2020, **17**, 6676-6698.
13. J. Siekmann, S. Ravishankar and T. Kirchartz, *ACS Energy Lett.,* 2021, **6**, 3244-3251.
14. M. De Keersmaecker, N. R. Armstrong, E. L. Ratcliff, *Energy Environ. Sci.*, 2021, **14**, 4840-4846.
15. R. A. Kerner, L. Zhao, S. P. Harvey, J. J. Berry, J. Schwartz and B. P. Rand, *ACS Energy Lett.*, 2020, **5**, 3352–3356.
16. R. A. Kerner, A. V. Cohen, Z. Xu, A. R. Kirmani, S. Y. Park, S. P. Harvey, J. P. Murphy, R. C. Cawthorn, N. C. Giebink, J. M. Luther, K. Zhu, J. J. Berry, L. Kronik and B. P. Rand, *Adv. Mater.*, 2023, **35**, 2302206.
17. A. J. Bard, R. Parsons and J. Jordan, *Standard Potentials in Aqueous Solution*, CRC Press, 1985, 294-312.